Nuclear Science and Techniques (2025) 36:163
https://doi.org/10.1007/s41365-025-01724-1

Optimization of the prompt fission neutron spectra of ^{239}Pu(n,f) via criticality benchmarking

Jia-Hao Chen[1] · Bo Yang[1] · Qing-Gang Jia[1] · Rui Li[2] · Wen-Di Chen[1] · Hai-Rui Guo[1] · Wei-Li Sun[1] · Tao Ye[1]

Received: 22 September 2024 / Revised: 20 January 2025 / Accepted: 26 January 2025 / Published online: 28 June 2025

Abstract
Prompt fission neutron spectra (PFNS) have a significant role in nuclear science and technology. In this study, the PFNS for ^{239}Pu are evaluated using both differential and integral experimental data. A method that leverages integral criticality benchmark experiments to constrain the PFNS data is introduced. The measured central values of the PFNS are perturbed by constructing a covariance matrix. The PFNS are sampled using two types of covariance matrices, either generated with an assumed correlation matrix and incorporating experimental uncertainties or derived directly from experimental reports. The joint Monte Carlo transport code is employed to perform transport simulations on five criticality benchmark assemblies by utilizing perturbed PFNS data. Extensive simulations result in an optimized PFNS that shows improved agreement with the integral criticality benchmark experiments. This study introduces a novel approach for optimizing differential experimental data through integral experiments, particularly when a covariance matrix is not provided.

Keywords Prompt fission neutron spectra · Differential nuclear data · Criticality benchmark · Random sample · Transport simulation

1 Introduction

Nuclear fission has been widely applied in nuclear engineering owing to the substantial energy release during this process. Despite the existence of several models that aid in understanding the mechanism of nuclear fission [1–6], current understanding of nuclear fission processes remains incomplete, both in terms of experimental observations and theoretical research [7–10]. Nuclear data serve as a fundamental basis for understanding the physical mechanisms of nuclear fission and its diverse applications in nuclear engineering. As an important fission nucleus, ^{239}Pu is widely used in accelerator-driven subcritical systems and fast neutron reactors [11, 12]. Therefore, nuclear data of the neutron-induced fission of ^{239}Pu have received extensive attention. Specifically, the prompt fission neutron spectra (PFNS) of neutron-induced ^{239}Pu fission have significant applications in reactor calculations, shielding, nuclear fuel management, and transmuting nuclear waste. This has inspired continuous interest in enhancing the accuracy of PFNS for these applications [13, 14].

PFNS measurement is a crucial task in nuclear physics and is commonly achieved through the use of a fission chamber combined with the neutron time-of-flight (TOF) technique. This method obtains the energy of fission neutrons by measuring the time difference between the time signals generated by the fission fragments and those of the emitted neutrons [15]. With the development of experimental detection techniques, several experiments have measured the different energy regions of the PFNS of ^{239}Pu(n, f) for various incident neutron energies [16–20]. However, experimental data often suffer from poor statistics and complex analyses, which can result in incomplete coverage of all energy domains, large uncertainties, and inconsistencies [16–20].

This work was supported by the National Natural Science Foundation of China (No.12347126).

✉ Bo Yang
yang_bo@iapcm.ac.cn

✉ Tao Ye
ye_tao@iapcm.ac.cn

[1] Institute of Applied Physics and Computational Mathematics, Beijing 100094, China

[2] CAEP Software Centre for High Performance Numerical Simulation (CAEP-SCNS), Beijing 100088, China

In practice, evaluated data are used in various engineering applications. The evaluation process typically involves both experimental data and theoretical calculations. Models such as the Maxwellian distribution, Watt spectrum, and Los Alamos model [21–23] are typically used for evaluation with the aim of providing evaluated data across the entire energy range. However, it is important to note that the current state of PFNS within evaluated nuclear data libraries is not yet fully satisfactory. Despite the existence of several international libraries, such as CENDL−3.2 [24], ENDF/B-VIII.0 [25], JENDL-5 [26], and JEFF−3.3 [27], inconsistencies in PFNS remain. This highlights the need for further research to enhance data accuracy and consistency.

The uncertainty in differential experimental data is often relatively large. The use of similar detection methods in most experiments can lead to unidentified biases or errors, resulting in incorrect evaluations of mean values and covariances [28]. Given that the measurement accuracy of physical quantities in integral experiments is often higher and directly related to practical applications, integral experimental data can be used to constrain differential experimental data. Several studies have aimed to provide guidance for improving evaluation data through integral experiments. These methods typically constrain microscopic data by simulating integral experiments, employing models to represent the microscopic data, and utilizing sensitivity analysis and Bayesian methods to adjust the microscopic data [28–31].

However, the uncertainties derived from the propagation of model parameter uncertainties in PFNS models tend to be smaller at certain outgoing energies, which is often inconsistent with the uncertainties typically observed in experimental PFNS. Furthermore, uncertainties attributable to the inherent shortcomings of the model are usually not estimated or included in the evaluation process [32–34]. To minimize the impact of the model on data optimization and circumvent the sensitivity analysis requirement that the integral quantity must exhibit a linear response to the differential quantity, this study perturbs the latest differential experimental data to generate a significant amount of PFNS data. Subsequently, the perturbed PFNS are then incorporated as inputs into a transport simulation. By comparing the calculated integral quantities k_{eff} for the criticality benchmarks, the quality of the perturbed PFNS is evaluated.

In general, perturbations can be performed based on the covariance matrix. However, the covariance matrix in experiments typically needs to be obtained through sufficient experimental information, such as counting statistics, background correction, detector efficiency determination, finite-time resolution, and uncertainty in the TOF length [35]. Furthermore, many studies have not clearly reported this information, particularly in early experiments.

Therefore, in this study, an assumed correlation matrix is combined with experimental uncertainties to generate a covariance matrix. Additionally, for comparative analysis, sampling is conducted using the covariance matrix provided by the experiment. This offers a novel approach for optimizing microscopic experimental data through integral experiments. Specifically, this method can be applied to optimize microscopic experimental data when a covariance matrix is not provided.

2 Methods

Considering the relatively large uncertainties associated with differential experiments, and taking into account the higher precision of integral experimental data, as well as the fact that criticality benchmark experiments have already been employed for validating and improving nuclear data [36, 37], alongside their similarity to engineering applications, this study aims to maximize the utilization of the existing experimental data. To achieve this aim, integral nuclear data k_{eff} were employed as the target quantity to constrain the microscopic nuclear data, specifically the PFNS of ^{239}Pu. The main approach involved using the differential experimental data and their associated uncertainty information to perturb the experimental values and then utilizing these perturbed data in transport simulations to determine the optimal differential data.

To minimize the impact of the models on this method, a data-driven approach was adopted to constrain the PFNS. As the Watt–Maxwellian function has four adjustable parameters, it exhibits flexibility in describing the PFNS [32, 38]. Consequently, the experimental data were typically well fitted by the Watt–Maxwellian function. The Watt–Maxwellian function was exclusively employed to describe the differential data, leveraging its properties of normalization and nonnegativity to ensure that the PFNS maintained the characteristics of the shape spectra and enabled the extrapolation of differential data beyond the available range. The Watt–Maxwellian function is a linear combination of the Maxwellian and Watt distributions:

$$\begin{aligned} f_{\mathrm{WM}}(E) &= w_{\mathrm{M}} f_{\mathrm{M}}\left(E, E_{\mathrm{M}}\right) + \left(1 - w_{\mathrm{M}}\right) f_{\mathrm{W}}\left(E, a_{\mathrm{W}}, b_{\mathrm{W}}\right) \\ f_{\mathrm{M}}\left(E, E_{\mathrm{M}}\right) &= K_{\mathrm{M}} \sqrt{E} e^{-E/E_{\mathrm{M}}} \\ f_{\mathrm{W}}\left(E, a_{\mathrm{W}}, b_{\mathrm{W}}\right) &= K_{\mathrm{W}} e^{-E/a_{\mathrm{W}}} \sinh \sqrt{b_{\mathrm{W}} E} \end{aligned} \tag{1}$$

where w_{M} is the weight of the Maxwellian function and w_{M}, E_{M}, a, and b are adjustable parameters that were used to fit the function. By fitting the differential experimental data, the PFNS was obtained in the form of a Watt–Maxwellian under different incident energies.

2.1 Generation of the perturbed PFNS

The differential experimental data used in this method were sourced from the experimental nuclear reaction database (EXFOR), as reported in [39, 40]. These studies have reported the latest experimental data on the neutron-induced PFNS of ^{239}Pu, covering 20 average incident energy points ranging from 1 to 20 MeV. Compared with the measurement results in the previous literature, this dataset has achieved breakthroughs in terms of accuracy, detailed uncertainty analysis, and thorough investigations of necessary corrections [39, 41].

By utilizing the experimental uncertainty information, a perturbation of the data around the experimental measurements is proposed to generate a perturbed PFNS for transport code simulations. However, owing to the large number of data points, a gridded approach for generating points, in which candidate values are generated at each energy point based on the mean values and error bars, significantly slows the calculation process as the computational load grows exponentially with the number of data points. To reduce computational cost, this study introduces a sampling method that utilizes a covariance matrix to reduce the dimensionality of data variations. This obtains a relatively optimized PFNS with fewer simulation calculations, thereby improving computational efficiency.

The EXFOR database often includes experimental data accompanied by uncertainties; however, covariance data are not always available. To develop a method applicable to general scenarios, particularly in the absence of a reported covariance matrix, a correlation matrix was constructed based on the characteristics observed in the correlation matrix in [39, 40], and a covariance matrix was generated by combining the uncertainty information from the experiments. The correlation matrix diagram [39, 40] showed an extremely high correlation between the PFNS at different neutron incident energies. Therefore, assuming that the correlation between different data points in the PFNS spectrum decreases exponentially with the square of their distance, as shown in Eq. 2, a covariance matrix was constructed and used to perturb each data point of the PFNS spectrum at a single incident energy.

$$\begin{aligned} \mathrm{cor}_{ij} &= e^{-\frac{d_{ij}^2}{2\sigma 2}} \\ d_{ij} &= |i - diag_j| \end{aligned} \tag{2}$$

where $diag_j$ represents the diagonal element coordinate in the jth row and i denotes the position of the ith element within the same jth row. The value of σ indicates the rate at which the correlation decreases as the distance increases. This assumption captures some of the patterns in the experimental data and effectively reduces the degrees of freedom for data perturbation.

To mitigate the impact of excessive uncertainty at low-energy points on the fitting function, data points were selected within an energy range consistent with those reported in the literature, specifically selecting points > 100 keV for outgoing neutron energies. Based on the above description, the total uncertainty was used as the standard deviation, which is the square root of the variance. The correlation definition provided in Eq. 3 [42] was used to obtain the covariance matrix. From this definition, it was simple to derive Eq. 4. The covariance matrix was computed by combining the derived equation with the assumed correlation matrix.

$$\begin{aligned} \mathrm{cor}_{ij} &= \frac{\mathrm{cov}_{ij}}{\sqrt{\mathrm{cov}_{ii}\mathrm{cov}_{jj}}} \\ \mathrm{var}_i &= \mathrm{cov}_{ii} \end{aligned} \tag{3}$$

$$\mathrm{cov}_{ij} = \mathrm{cor}_{ij}\sqrt{\mathrm{cov}_{ii}\mathrm{cov}_{jj}} \tag{4}$$

where var denotes the variance vector, cor_{ij} represents the element in the ith column and jth row of the correlation matrix, and cov_{ij} represents the element in the ith column and jth row of the covariance matrix. Using the generated covariance matrix, the differential experimental data were perturbed, thereby producing PFNS discrete points proximal to the differential experimental data. As the new PFNS were obtained through sampling, it did not inherently possess the properties of a shaped spectrum. To address this, the Watt–Maxwellian function was employed to fit the perturbed data to generate a continuous, normalized, and nonnegative PFNS. The fitting results are shown in Fig. 1.

As depicted in Fig. 1, random sampling utilizing the covariance matrix effectively generated perturbed data proximal to the experimental data, and the Watt–Maxwellian function exhibited a robust fit to the perturbed data points. For a comprehensive set of PFNS encompassing various incident energies, a strong correlation across PFNS at different incident energies was achieved by selecting a uniform random number seed. This novel sampling and fitting methodology yielded a substantial number of continuous PFNS.

2.2 Using the perturbed data for transport calculations

To correlate differential data with integral data, transport calculations were used, taking differential data as the input and generating integral data as the output, which was then compared with the benchmarks. In this study, the joint Monte Carlo transport (JMCT) code was utilized to perform criticality computations [43–45].

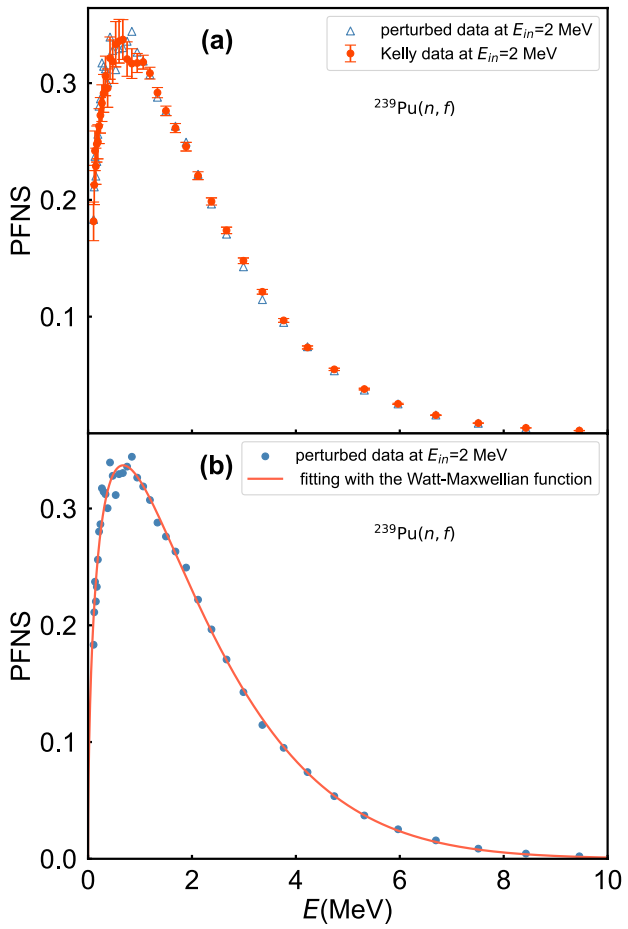

Fig. 1 (Color Online) PFNS of ^{239}Pu(n, f) for **a** perturbed data, shown by blue hollow triangles, in comparison with the literature values shown by red points [39], and **b** perturbed data, shown by blue points, along with the fitting result to the data

To optimize the PFNS, during transport calculations, except for the PFNS data, all other nuclear data were obtained from the ENDF/B-VIII.0 library [25]. To generate PFNS data suitable for utilization in this code, a nuclear data processing system (NJOY2016) was used to process the perturbed PFNS data, transforming them into the ACE format [46]. To facilitate subsequent comparisons with the results from ENDF/B-VIII.0, the same incident energy selections as those in ENDF/B-VIII.0 were adopted. As the experimental data did not perfectly align with this set of incident energies, linear interpolation was used to generate PFNS for various incident energies. As the range of the experimental incident energies was slightly narrower than that of ENDF/B-VIII.0, the PFNS was extrapolated for energies below the minimum experimental average incident energy of 1.54 MeV or above the maximum experimental incident energy of 19.59 MeV in ENDF/B-VIII.0. Specifically, a consistent approach of linear extrapolation, analogous to the aforementioned linear interpolation method, was used to predict PFNS at these incident energies.

Given that the differential experimental data employed in this study were limited to the incident energy range > 1 MeV, the selection of fast neutron spectra was the most appropriate for this specific energy domain. To minimize the possible uncertainty in the transport process while covering as much of the experimental data region as possible, five criticality benchmarks with relatively simple geometric configurations were selected. Each of these benchmarks is characterized by a dominant "FAST" flux spectrum and is directly associated with the nuclide ^{239}Pu. The benchmark cases employed in this study were Pu-Met-Fast-002, Pu-Met-Fast-003, Pu-Met-Fast-008, Pu-Met-Fast-009, and Pu-Met-Fast-010 [47, 48]. In the aforementioned benchmarks, Pu-Met-Fast-002 represents a bare experiment (20.1 at.% ^{240}Pu), Pu-Met-Fast-003 represents an array of plutonium metal buttons in an unmoderated configuration, Pu-Met-Fast-008 represents an experiment involving a thorium reflector, Pu-Met-Fast-009 represents an aluminum reflected experiment, and Pu-Met-Fast-010 represents an experiment that utilizes a natural uranium reflector [49]. By utilizing these relatively simple criticality benchmark assemblies, which encompass diverse configurations, this study aimed to enhance the robustness of the constraints on differential data by integrating the experimental data. The input for the JMCT used computer-aided design (CAD) modeling [45], and the models of these criticality benchmarks were constructed based on information sourced from the MIT Computational Reactor Physics Group [50].

All cases were executed using the same perturbed data, with each simulation using 10000 neutrons per cycle, 100 inactive cycles, and 1400 additional active cycles. The uncertainty of the calculated eigenvalue k_{eff} exhibited a slight variability depending on the device and input files; however, it consistently remained < 20 pcm. This value is notably smaller than the benchmark uncertainties.

2.3 Calculated δk_{eff}

To evaluate the quality of each perturbed PFNS, a comparative analysis was conducted between the eigenvalues k_{eff} derived from transport simulations for the five criticality benchmarks and their respective benchmark values. Specifically, the relative calculation-to-experimental ratio, denoted as $\frac{|C-E|}{E}$, was used to quantitatively assess the deviation between the calculated and benchmark k_{eff} values sourced from [47]. Notably, the benchmark k_{eff} values for these benchmark integral experiments were all 1.000. The relative difference between the calculated and experimental values is given by Eq. 5, where $k_{\mathrm{eff},b}^{\mathrm{cal}}$ represents the calculated k_{eff} for the b-th criticality benchmark assembly, and $k_{\mathrm{eff},b}^{\mathrm{ben}}$ represents the benchmark value of k_{eff} for the same assembly.

Furthermore, the total relative difference was introduced, denoted by $\delta k_{\text{eff}}^{\text{tot}}$, which was defined as the average of $\delta k_{\text{eff},b}$ calculated for all criticality benchmarks, as outlined in Eq. 6.

This approach enabled the identification of the most suitable perturbed PFNS that best captured the integral experimental behavior and achieved optimal results.

$$\delta k_{\text{eff},b} = \frac{|k_{\text{eff},b}^{\text{cal}} - k_{\text{eff},b}^{\text{ben}}|}{k_{\text{eff},b}^{\text{ben}}} \tag{5}$$

$$\delta k_{\text{eff}}^{\text{tot}} = \frac{\sum_b \delta k_{\text{eff},b}}{5} \tag{6}$$

To clarify the entire process of utilizing the integral experimental data to constrain the differential experimental data, a flowchart was created for the aforementioned method, which is presented in Fig. 2. By sampling from the covariance matrix, the perturbed PFNS were obtained that were distributed near the differential experimental data. These perturbed PFNS were then processed using the NJOY code to generate data in ACE format. For each set of perturbed PFNS, JMCT was employed to perform transport simulations on the five criticality benchmarks. Through extensive simulations, the perturbed PFNS were identified that not only exhibited the closest alignment with the benchmark values but also maintained close proximity to the original differential experimental data. This approach ensured a robust and reliable method for constraining differential experimental data using integral experimental information, ultimately enhancing the accuracy and applicability of differential experimental data.

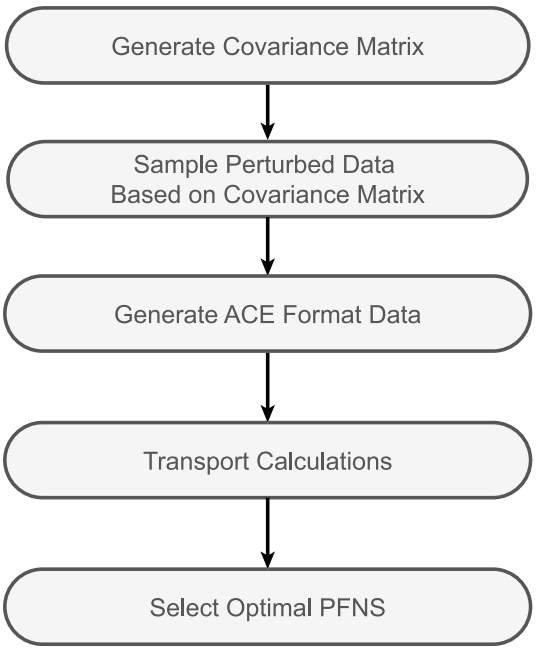

Fig. 2 Flowchart of optimizing the differential PFNS process through the use of integral experiments

3 Results and discussion

3.1 Calculation results from the generated covariance matrix

By following the steps shown in Fig. 2, a covariance matrix was initially generated based on Eq. 2, assuming that $\sigma = 1$. This assumption allowed the derivation of a correlation matrix that exhibited a relatively rapid decrease in the correlation between data points. By incorporating the uncertainty data provided in the experiment [40], the covariance matrix was obtained for this specific scenario. Subsequently, this covariance matrix was used to perform random sampling of the data points, thereby generating perturbed datasets. In this framework, 1,000 samplings were executed and the corresponding $\delta k_{\text{eff}}^{\text{tot}}$ values for each sampling were calculated. This process ultimately yielded a distribution of $\delta k_{\text{eff}}^{\text{tot}}$, as shown in Fig. 3.

Figure 3a illustrates the effect of the PFNS sampled from the generated covariance data on the transport calculations. The scattered random distribution of points reflects the stochastic nature of the sampling process. It is evident that different PFNS lead to variations in the computed k_{eff} values, demonstrating that adjustments to the differential data within the error bands can affect the integral data. This further validates the effectiveness of constraining differential experiments through integral experiments. Figure 3b shows a histogram of the statistical distribution of $\delta k_{\text{eff}}^{\text{tot}}$, which shows a rapid decrease at both ends of the distribution. The red Gaussian function fitting line in Fig. 3b shows that as $\delta k_{\text{eff}}^{\text{tot}}$ decreased, its statistical distribution exhibited exponential decay. This suggests that the current sampling, with $\sigma = 1.0$, is statistically sufficient for obtaining the optimal value. Additionally, Fig. 3b shows that optimizing the calculation of k_{eff} by adjusting only the PFNS method ultimately leads to an optimal value of $\delta k_{\text{eff}}^{\text{tot}}$ of approximately 0.002. The optimal PFNS obtained through sampling corresponds to a $\delta k_{\text{eff}}^{\text{tot}}$ value of 0.00219. When the calculations were performed using the ENDF/B-VIII.0 library, the resulting $\delta k_{\text{eff}}^{\text{tot}}$ value was 0.00299. This comparison indicates that the PFNS that is perturbed using the latest experimental data performs better in integral experimental validation than the PFNS in the ENDF/B-VIII.0 library.

To broaden the scope of the parameter variation, different values for σ were selected in Eq. 2. By choosing distinct σ values, the rate of decrease in the correlation for the correlation matrix was altered, thereby generating different covariance matrices. In addition, $\sigma = 0.1$, 0.2, 0.5, 1.5, 2.0, and 5.0 were selected and the method detailed in Sect. 2

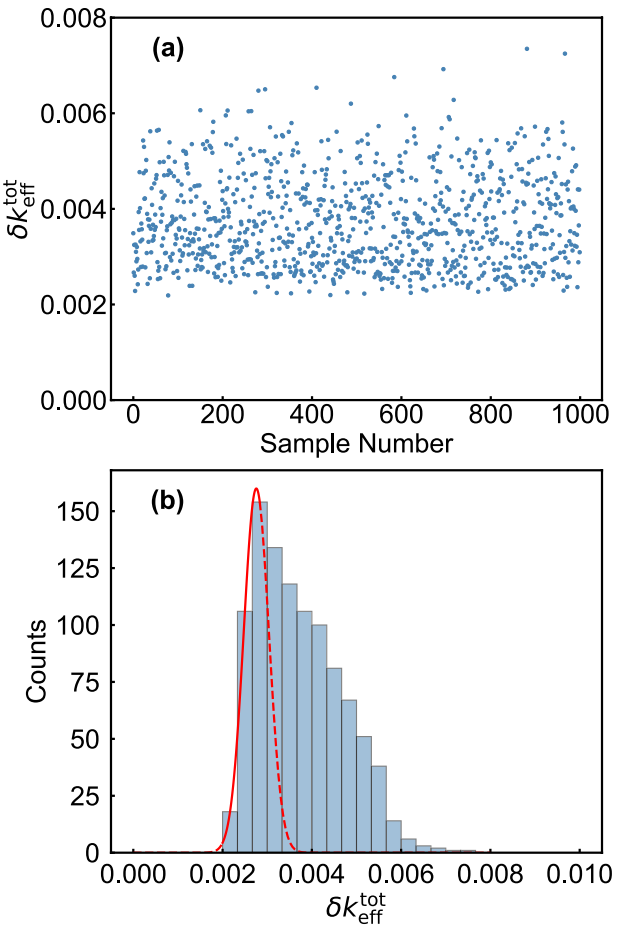

Fig. 3 (Color Online) Assuming $\sigma = 1.0$, the distribution of $\delta k_{\rm eff}^{\rm tot}$ obtained by comparing the transport calculated results with the benchmark values is shown as follows: **a** a two-dimensional plot of $\delta k_{\rm eff}^{\rm tot}$ versus the sample number; **b** a histogram of the statistical distribution of $\delta k_{\rm eff}^{\rm tot}$. The red line represents a Gaussian function fit to the histogram in the range of $\delta k_{\rm eff}^{\rm tot} = 0.002$ to 0.003, and the red solid line indicates the fitting range

was used to generate the covariance matrices. Analogous to the case where $\sigma = 1.0$, $\delta k_{\rm eff}^{\rm tot}$ was computed for a range of σ values. Owing to variations in the covariance matrix, the distribution of the computed $\delta k_{\rm eff}^{\rm tot}$ also exhibited differences. For each value of σ, 1000 samples were taken, and $\delta k_{\rm eff}^{\rm tot}$ was calculated based on the perturbed PFNS generated by sampling, as shown in Fig. 4.

As illustrated in Fig. 4, although the distribution of $\delta k_{\rm eff}^{\rm tot}$ varied under different σ values, its main characteristics remained consistent as the distribution of $\delta k_{\rm eff}^{\rm tot}$ decreased rapidly at both ends. Notably, at the left end of the horizontal axis as shown in Fig. 4, all cases exhibited the same characteristics as when $\sigma = 1.0$, that is, as the value of $\delta k_{\rm eff}^{\rm tot}$ on the x-axis in Fig. 4 decreased, its statistics decreased exponentially, converging to approximately 0.002. This indicates that the results obtained using a sample size of 1000 are sufficient to represent the distribution of $\delta k_{\rm eff}^{\rm tot}$. Although a larger sample size would yield results closer to the optimal value when sampling methods are used to obtain the best PFNS, the current sample size provided a satisfactory approximation.

The perturbed PFNS have been obtained for seven distinct σ values. The results were compiled together to use the statistical information from the entire sampling process. The overall distribution of $\delta k_{\rm eff}^{\rm tot}$ obtained from all sampling results is shown in Fig. 5. In the cases of the various σ values mentioned earlier, the distribution of $\delta k_{\rm eff}^{\rm tot}$ decreased rapidly at both ends and exhibited an exponentially decreasing trend at the low $\delta k_{\rm eff}^{\rm tot}$ end and converged to approximately 0.002. To synthesize the previous data, Fig. 5 naturally exhibits such characteristics in its distribution of $\delta k_{\rm eff}^{\rm tot}$. However, owing to improvements in the statistics and superposition of various σ cases, the statistical fluctuations of the distribution decreased, resulting in a more continuous distribution. The optimal $\delta k_{\rm eff}^{\rm tot}$ obtained for all perturbed PFNS generated using the method based on covariance matrix creation and sampling was 0.00210. This value is very close to the optimal $\delta k_{\rm eff}^{\rm tot}$ previously obtained by considering only the case where $\sigma = 1.0$, which also indicates a rapid decrease in $\delta k_{\rm eff}^{\rm tot}$ at the low $\delta k_{\rm eff}^{\rm tot}$ end.

3.2 Calculation results from the experimental covariance matrix

In recent years, with the growing emphasis on covariance data in experiments and evaluations, more experiments have begun to report covariance data. The experimental data used in this study included a reported covariance matrix [39, 40]. The reported covariance matrix from the experiment was used to generate a perturbed PFNS using the aforementioned sampling method. This specific method is consistent with that described in Sect. 2, with the only modification being the replacement of covariance matrix generation. 600 samplings were performed using the covariance data provided by the experiment, and the $\delta k_{\rm eff}^{\rm tot}$ values were calculated based on each perturbed PFNS. The distribution of $\delta k_{\rm eff}^{\rm tot}$ calculated using the PFNS sampled based on the experimental covariance matrix is shown in Fig. 6. This distribution exhibited a relatively higher probability at lower $\delta k_{\rm eff}^{\rm tot}$ values, which is beneficial for achieving faster convergence to the optimal value of $\delta k_{\rm eff}^{\rm tot}$. The optimal PFNS obtained through this sampling method, utilizing the covariance matrix, was directly derived from the experiment, yielding a $\delta k_{\rm eff}^{\rm tot}$ of 0.00208, which was slightly better than previous results.

3.3 Discussion

Covariance matrices were generated for the differential data using two distinct methods. Method 1 involved constructing a correlation matrix and combining it with the

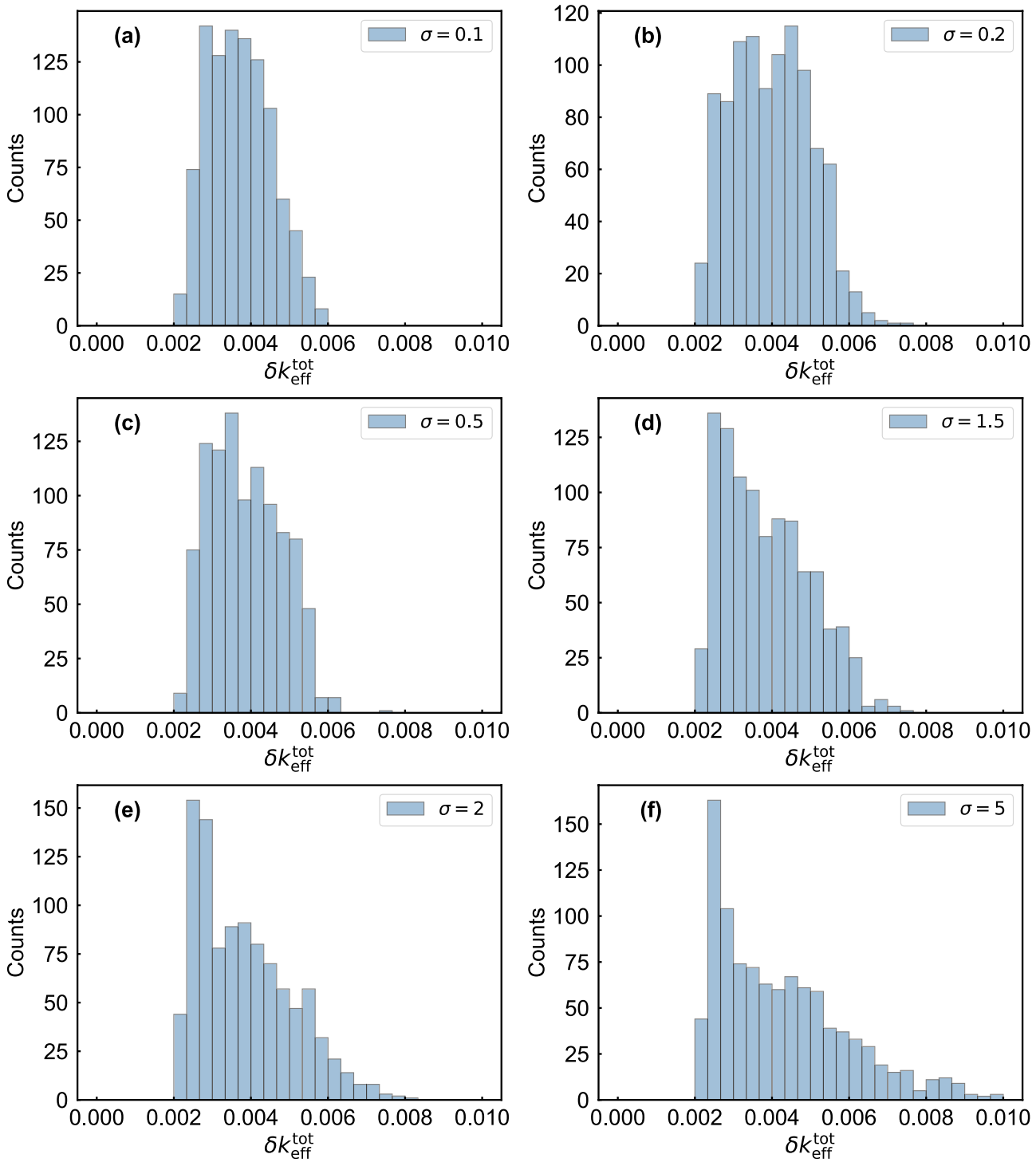

Fig. 4 (Color online) Distribution of $\delta k_{\mathrm{eff}}^{\mathrm{tot}}$ obtained by comparing the transport calculated results with the benchmark values under the following cases: **a** $\sigma = 0.1$; **b** $\sigma = 0.2$; **c** $\sigma = 0.5$; **d** $\sigma = 1.5$; **e** $\sigma = 2.0$; **f** $\sigma = 5.0$

experimental uncertainty information. Method 2 directly utilized the covariance information provided by the experiment. The experimental data were perturbed near the error range through random sampling, and the perturbed PFNS were used for transport calculations to conduct integral validation, thereby optimizing the differential PFNS.

Based on the results presented in Figs. 5 and 6, the distributions of $\delta k_{\mathrm{eff}}^{\mathrm{tot}}$ produced by the perturbed PFNS

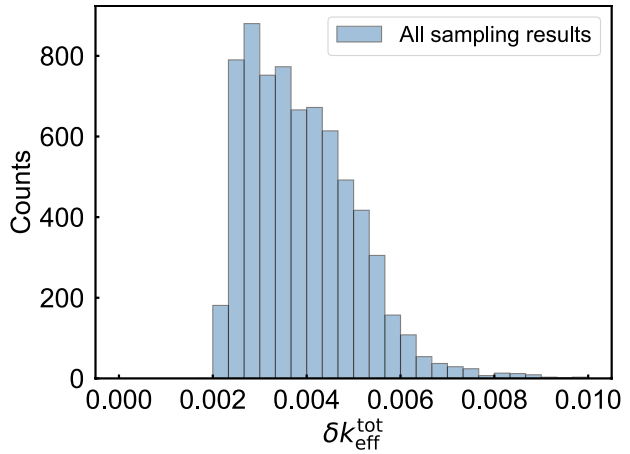

Fig. 5 (Color online) Distribution of $\delta k_{\text{eff}}^{\text{tot}}$ across all sampling results, including those with σ = 0.1, 0.2, 0.5, 1.0, 1.5, 2.0, and 5.0, totaling 7000 samples

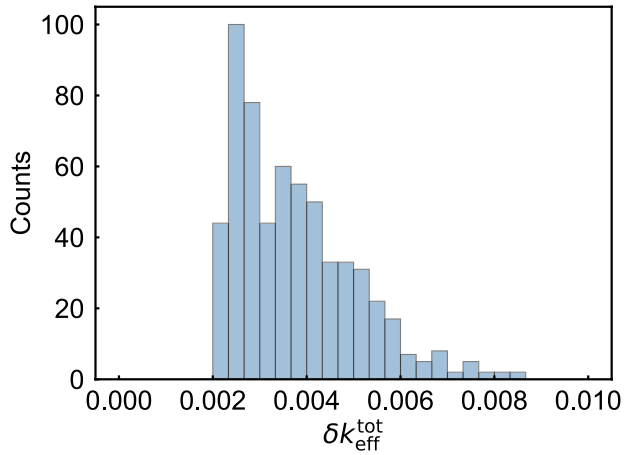

Fig. 6 (Color online) Distribution of $\delta k_{\text{eff}}^{\text{tot}}$ calculated using the perturbed PFNS sampled from the experimental covariance matrix

Table 1 Comparison between the optimal $\delta k_{\text{eff}}^{\text{tot}}$ values obtained through sampling using two methods for generating covariance matrices, and the $\delta k_{\text{eff}}^{\text{tot}}$ values calculated based on ENDF/B-VIII.0

PFNS Source	Method 1	Method 2	ENDF/B-VIII.0
$\delta k_{\text{eff}}^{\text{tot}}$	0.00210	0.00208	0.00299

obtained using both methods exhibited rapid decreases at low $\delta k_{\text{eff}}^{\text{tot}}$ values. The optimal PFNS values converged using the two methods were not significantly different. The results are listed in Table 1, which demonstrates that the optimized PFNS obtained through the random sampling method performed better in integral experiments than the PFNS provided by ENDF/B-VIII.0. Furthermore, Figs. 5 and 6 show that, at the left end of the $\delta k_{\text{eff}}^{\text{tot}}$ distribution,

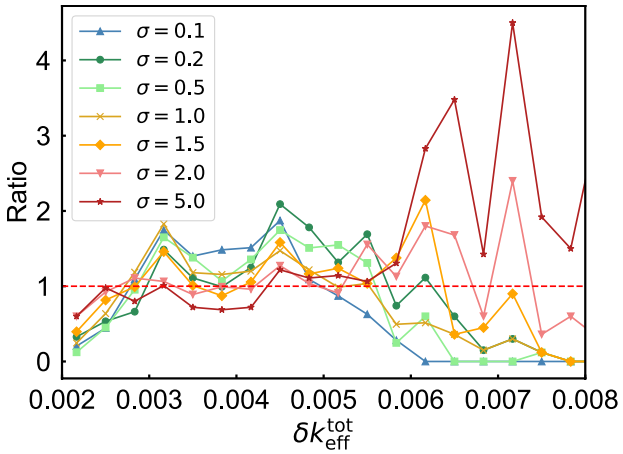

Fig. 7 (Color Online) Ratios represent the comparison between the normalized distribution of $\delta k_{\text{eff}}^{\text{tot}}$ obtained under varying σ values using Method 1, and the normalized distribution of $\delta k_{\text{eff}}^{\text{tot}}$ calculated through covariance sampling derived from experimental data, denoted as Method 2. The red horizontal dashed line indicates a ratio of 1

it converged to a value near 0.002, rather than 0. This implies that merely adjusting the PFNS may not be sufficient to obtain a k_{eff} calculation value that is identical to the benchmark. However, a relatively better PFNS can still be obtained using this method.

Although methods 1 and 2 can optimize the PFNS to approach an optimal value, differences in the covariance matrix lead to varying convergence speeds of the data near this optimal value. The distribution characteristics near a low $\delta k_{\text{eff}}^{\text{tot}}$ can be described by comparing the ratios of the distributions obtained using methods 1 and 2. Specifically, the distribution generated by Method 2 was used as the standard and the distribution histograms of $\delta k_{\text{eff}}^{\text{tot}}$ were compared under different σ values in Method 1 with those in Fig. 6 by calculating their ratios. Specifically, after normalizing Fig. 3, Fig. 4a–f is used to calculate the ratios with the normalized histogram of Fig. 6 for each bin within the range of $\delta k_{\text{eff}}^{\text{tot}} = 0.002 \sim 0.008$ to obtain Fig. 7. The horizontal coordinates of the points indicated in Fig. 7 show the center values of the bins.

Figure 7 illustrates that, near the left end of the $\delta k_{\text{eff}}^{\text{tot}}$ distribution, the ratio of the distribution of $\delta k_{\text{eff}}^{\text{tot}}$ obtained from all samples in Method 1 to the distribution derived from Method 2 was < 1. This suggests that the covariance provided by the experimental data was more suitable for sampling to obtain the optimal PFNS. However, it should be noted that in cases where experimental covariance data are missing, Method 1, which constructs a correlation matrix combined with experimental uncertainty information to generate a covariance matrix for sampling, can also effectively approximate the optimal value. However, compared with Method 2, it exhibited a relatively lower efficiency near the

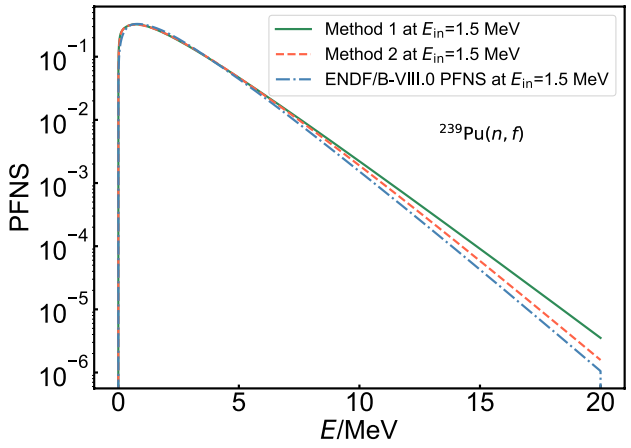

Fig. 8 (Color Online) Comparison of the optimized PFNS of ^{239}Pu(n,f) results obtained using Methods 1 and 2 with ENDF/B-VIII.0, illustrated using an incident energy of 1.5 MeV as a representative example

optimal value. This observation aligns with the results presented in Table 1, demonstrating that Method 2 achieves a better PFNS with fewer sampling instances.

Figure 8 presents a comparison of the optimized PFNS results obtained using Methods 1 and 2 with ENDF/B-VIII.0, using an incident energy of 1.5 MeV as an example. The optimized PFNS exhibited slight variations from ENDF/B-VIII.0, and these variations contributed to the optimization of the integral experiment for calculating k_{eff}. As illustrated in Fig. 8, the method of utilizing integral experiments to constrain differential experiments demonstrates an effective adjustment of PFNS. Owing to the normalization of the spectrum, there is inevitably an interplay between the low- and high-count parts of the final energy spectrum, and the distribution in the low-count region is modulated by slight variations in the high-count region. The results show that the adjusted PFNS performs better in calculating the criticality benchmarks. Consequently, the adjustment to the PFNS is beneficial for the entire spectrum, as it aligns well with both the microscopic and integral experiments.

4 Summary and prospects

In summary, a method was introduced that utilizes integral criticality benchmark experiments to constrain the data of differential quantities, specifically the PFNS. The measured central values were perturbed by constructing a correlation matrix and combining it with the experimental error data provided by experiments. Subsequently, the perturbed PFNS was used as the input data for transport simulations. The quality of the perturbed PFNS was evaluated by comparing the deviation between the calculated k_{eff} and the benchmark values of the criticality assemblies. A set of optimal PFNS values was obtained through extensive sampling. In addition, this study examined a sampling method based on a covariance matrix derived from differential experiments. The results indicate that sampling using the covariance matrix directly provided by the experiments yields a higher probability of obtaining results close to the optimal value, thereby facilitating the achievement of a better PFNS with fewer sampling instances. Notably, in terms of the optimal value, the method for generating a covariance matrix using an assumed correlation matrix is similar to the method that utilizes the experimentally provided covariance matrix. This indicates that, for data lacking an experimentally provided covariance matrix, the proposed method can still be utilized to obtain a relatively optimized PFNS through a finite number of sampling iterations.

It is also important to note that the optimal $\delta k_{\mathrm{eff}}^{\mathrm{tot}}$ obtained was close to but not equal to zero, at approximately 0.002. Furthermore, based on the distribution of $\delta k_{\mathrm{eff}}^{\mathrm{tot}}$ obtained from the sampling iteration and the observed decreasing trend at low $\delta k_{\mathrm{eff}}^{\mathrm{tot}}$, it can be inferred that simply adjusting the PFNS of ^{239}Pu is insufficient to make the k_{eff} value calculated from the transport calculations identical to the benchmark value. This is due to the existence of other microscopic quantities that affect k_{eff}, such as the cross sections, and prompt neutron multiplicities of the neutron-induced reaction of ^{239}Pu. This study further suggests that the mutual constraints between multiple physical quantities can be achieved using criticality benchmark experiments. Moreover, owing to the added constraints of the integral data, this method is beneficial for evaluating differential quantities that lack experimental data. Additionally, it facilitates consistency between microscopic and macroscopic experimental data.

Author contributions All authors contributed to the study conception and design. Material preparation, data collection, and analysis were performed by Jia-Hao Chen, Qing-Gang Jia, and Tao Ye. The first draft of the manuscript was written by Jia-Hao Chen, and all authors commented on previous versions of the manuscript. All authors read and approved the final manuscript.

Data availability The data that support the findings of this study are openly available in Science Data Bank at https://cstr.cn/31253.11.sciencedb.j00186.00638 and https://doi.org/10.57760/sciencedb.j00186.00638.

Declarations

Conflict of interest The authors declare that they have no conflict of interest.

References

1. J.C. Pei, W. Nazarewicz, J.A. Sheikh et al., Fission barriers of compound superheavy nuclei. Phys. Rev. Lett. **102**, 192501 (2009). https://doi.org/10.1103/PhysRevLett.102.192501

2. W. Younes, D.M. Gogny, J. Berger, A microscopic theory of fission dynamics based on the generator coordinate method. Lect. Notes Phys. (2019). https://doi.org/10.1007/978-3-030-04424-4
3. X.M. Shi, G.L. Wang, K.J. Luo et al., Geant4 development for actinides photofission simulation. Nucl. Instrum. Methods Phys. Res. A **1062**, 169222 (2024). https://doi.org/10.1016/j.nima.2024.169222
4. G.L. Wang, H.Y. Lan, X.M. Shi et al., A general framework for describing photofission observables of actinides at an average excitation energy below 30 MeV. Chin. Phys. C **46**, 084102 (2022). https://doi.org/10.1088/1674-1137/ac6abc
5. Y. Su, Z.Y. Li, L.L. Liu et al., Sensitivity impacts owing to the variations in the type of zero-range pairing forces on the fission properties using the density functional theory. Nucl. Sci. Tech. **35**, 62 (2024). https://doi.org/10.1007/s41365-024-01422-4
6. N. Schunck, D. Regnier, Theory of nuclear fission. Prog. Part. Nucl. Phys. **125**, 103963 (2022). https://doi.org/10.1016/j.ppnp.2022.103963
7. X.J. Sun, C.G. Yu, N. Wang et al., Pre-neutron-emission mass distributions for reaction ^{238}U(n, f) up to 60 MeV. Chin. Phys. C **39**, 014102 (2015). https://doi.org/10.1088/1674-1137/39/1/014102
8. X.L. Yang, C.L. Lan, Y.B. Nie et al., Cumulative fission yield measurements with 14.7 MeV neutrons on ^{238}U. Chin. Phys. C **47**, 024001 (2023). https://doi.org/10.1088/1674-1137/aca1ab
9. C. Bhatia, B.F. Fallin, M.E. Gooden et al., Exploratory study of fission product yields of neutron-induced fission of ^{235}U,^{238} U, and ^{239}Pu at 8.9 MeV. Phys. Rev. C **91**, 064604 (2015). https://doi.org/10.1103/PhysRevC.91.064604
10. A. Bulgac, S. Jin, I. Stetcu, Nuclear fission dynamics: Past, present, needs, and future. Front. Phys. **8**, 63 (2020). https://doi.org/10.3389/fphy.2020.00063
11. B. Liu, X. Zhang, F. Liu et al., The electron accelerator driven sub-critical system. Nucl. Eng. Des. **386**, 111567 (2022). https://doi.org/10.1016/j.nucengdes.2021.111567
12. Y. Peneliau, O. Litaize, P. Archier et al., ^{239}Pu prompt fission neutron spectra impact on a set of criticality and experimental reactor benchmarks. Nucl. Data Sheets **118**, 459–462 (2014). https://doi.org/10.1016/j.nds.2014.04.106
13. D. Neudecker, T. Taddeucci, R. Haight et al., The need for precise and well-documented experimental data on prompt fission neutron spectra from neutron-induced fission of ^{2}39Pu. Nucl. Data Sheets **131**, 289–318 (2016). https://doi.org/10.1016/j.nds.2015.12.005
14. X. Zou, L. Cao, Q. Teng et al., Uncertainty propagation of prompt fission neutron spectrum for physics analysis of fast and thermal reactors. Prog. Nucl. Energy **144**, 104077 (2022). https://doi.org/10.1016/j.pnucene.2021.104077
15. T. Ethvignot, M. Devlin, R. Drosg et al., Prompt-fission-neutron average energy for ^{238}U(n, f) from threshold to 200 MeV. Phys. Lett. B **575**, 221–228 (2003). https://doi.org/10.1016/j.physletb.2003.09.048
16. P. Staples, J. Egan, G. Kegel et al., Prompt fission neutron energy spectra induced by fast neutrons. Nucl. Phys. A **591**, 41–60 (1995). https://doi.org/10.1016/0375-9474(95)00119-L
17. P. Talou, B. Becker, T. Kawano et al., Advanced Monte Carlo modeling of prompt fission neutrons for thermal and fast neutron-induced fission reactions on ^{239}Pu. Phys. Rev. C **83**, 064612 (2011). https://doi.org/10.1103/PhysRevC.83.064612
18. A. Chatillon, G. Bélier, T. Granier et al., Measurement of prompt neutron spectra from the ^{239}Pu(n,f) fission reaction for incident neutron energies from 1 to 200 MeV. Phys. Rev. C **89**, 014611 (2014). https://doi.org/10.1103/PhysRevC.89.014611
19. J. Lestone, E. Shores, Uranium and plutonium average Prompt-fission Neutron Energy Spectra (PFNS) from the analysis of NTS NUEX data. Nucl. Data Sheets **119**, 213–216 (2014). https://doi.org/10.1016/j.nds.2014.08.059
20. P. Marini, J. Taieb, B. Laurent et al., Prompt-fission-neutron spectra in the ^{239}Pu(n, f) reaction. Phys. Rev. C **101**, 044614 (2020). https://doi.org/10.1103/PhysRevC.101.044614
21. J. Terrell, Fission neutron spectra and nuclear temperatures. Phys. Rev. **113**, 527–541 (1959). https://doi.org/10.1103/PhysRev.113.527
22. B.E. Watt, Energy spectrum of neutrons from thermal fission of ^{235} U. Phys. Rev. **87**, 1037–1041 (1952). https://doi.org/10.1103/PhysRev.87.1037
23. D.G. Madland, J.R. Nix, New calculation of prompt fission neutron spectra and average prompt neutron multiplicities. Nucl. Sci. Eng. **81**, 213–271 (1982). https://doi.org/10.13182/NSE82-5
24. Z.G. Ge, R.R. Xu, H.C. Wu et al., CENDL-3.2: The new version of Chinese general purpose evaluated nuclear data library. EPJ Web Conf. **239**, 09001 (2020). https://doi.org/10.1051/epjconf/202023909001
25. D. Brown, M. Chadwick, R. Capote et al., ENDF/B-VIII.0: The 8th major release of the nuclear reaction data library with CIELO-project cross sections, new standards and thermal scattering data. Nucl. Data Sheets **148**, 1–142 (2018). https://doi.org/10.1016/j.nds.2018.02.001
26. O. Iwamoto, N. Iwamoto, S. Kunieda et al., Japanese evaluated nuclear data library version 5: JENDL-5. J. Nucl. Sci. Technol. **60**, 1–60 (2023). https://doi.org/10.1080/00223131.2022.2141903
27. A.J.M. Plompen, The joint evaluated fission and fusion nuclear data library. JEFF-3.3. Eur. Phys. J. A **56**, 181 (2020). https://doi.org/10.1140/epja/s10050-020-00141-9
28. P. Talou, T. Kawano, M.B. Chadwick et al., Uncertainties in nuclear fission data. J. Phys. G Nucl. Part. Phys. **42**, 034025 (2015). https://doi.org/10.1088/0954-3899/42/3/034025
29. G. Palmiotti, M. Salvatores, G. Aliberti et al., Combined use of integral experiments and covariance data. Nucl. Data Sheets **118**, 596–636 (2014). https://doi.org/10.1016/j.nds.2014.04.145
30. D. Neudecker, M. Grosskopf, M. Herman et al., Enhancing nuclear data validation analysis by using machine learning. Nucl. Data Sheets **167**, 36–60 (2020). https://doi.org/10.1016/j.nds.2020.07.002
31. I. Kodeli, A. Trkov, R. Capote et al., Evaluation and use of the prompt fission neutron spectrum and spectra covariance matrices in criticality and shielding. Nucl. Instrum. Methods Phys. Res. A **610**, 540–552 (2009). https://doi.org/10.1016/j.nima.2009.08.076
32. R. Capote, Y.J. Chen, F.J. Hambsch et al., Prompt fission neutron spectra of actinides. Nucl. Data Sheets **131**, 1–106 (2016). https://doi.org/10.1016/j.nds.2015.12.002
33. D. Neudecker, R. Capote, H. Leeb, Impact of model defect and experimental uncertainties on evaluated output. Nucl. Instrum. Methods Phys. Res. A **723**, 163–172 (2013). https://doi.org/10.1016/j.nima.2013.05.005
34. R. Capote, D. Smith, A. Trkov, Nuclear data evaluation methodology including estimates of covariances. EPJ Web Conf. **8**, 04001 (2010). https://doi.org/10.1051/epjconf/20100804001
35. D. Neudecker, P. Talou, T. Taddeucci et al., Preliminary evaluation and uncertainty quantification of the prompt fission neutron spectrum of ^{239}Pu. Nucl. Data Sheets **123**, 146–152 (2015). https://doi.org/10.1016/j.nds.2014.12.026
36. Y.Y. Ding, Y.B. Nie, Y. Zhang et al., Benchmark experiment on slab ^{238}U with D-T neutrons for validation of evaluated nuclear data. Nucl. Sci. Tech. **35**, 29 (2024). https://doi.org/10.1007/s41365-024-01386-5
37. Q. Zhao, Y.B. Nie, Y.Y. Ding et al., Measurement and simulation of the leakage neutron spectra from Fe spheres bombarded with 14 MeV neutrons. Nucl. Sci. Tech. **34**, 182 (2023). https://doi.org/10.1007/s41365-023-01329-6
38. A. Trkov, R. Capote, V. Pronyaev, Current issues in nuclear data evaluation methodology: ^{235}U prompt fission neutron spectra and

multiplicity for thermal neutrons. Nucl. Data Sheets **123**, 8–15 (2015). https://doi.org/10.1016/j.nds.2014.12.003
39. K.J. Kelly, M. Devlin, J.M. O'Donnell et al., Measurement of the ^{239} Pu (n, f) prompt fission neutron spectrum from 10 keV to 10 MeV induced by neutrons of energy 1–20 MeV. Phys. Rev. C **102**, 034615 (2020). https://doi.org/10.1103/PhysRevC.102.034615
40. K.J. Kelly, J.M. O'Donnell, M. Devlin, The Covariance of PFNS Results from the Chi-Nu Experiment. EPJ Web Conf. **281**, 00026 (2023). https://doi.org/10.1051/epjconf/202328100026
41. K.J. Kelly, P. Marini, J. Taieb et al., Comparison of results from recent NNSA and CEA measurements of the ^{239}Pu(n, f) prompt fission neutron spectrum. Nucl. Data Sheets **173**, 42–53 (2021). https://doi.org/10.1016/j.nds.2021.04.003
42. K.J. Kelly, J.M. O'Donnell, D. Neudecker et al., The analysis of shape data including normalization and the impact on prompt fission neutron spectrum measurements. Nucl. Instrum. Methods Phys. Res., Sect. A **943**, 162449 (2019). https://doi.org/10.1016/j.nima.2019.162449
43. L. Deng, G. Li, B.Y. Zhang et al., JMCT Monte Carlo Code with Capability of Integrating Nuclear System Feedback, in *Proceedings of the 2018 2nd International Conference on Applied Mathematics, Modelling and Statistics Application (AMMSA 2018)*, pp. 48-54, (2018), https://doi.org/10.2991/ammsa-18.2018.10
44. L. Deng, Z.H. Hu, R. Li et al., The coupled neutron transport calculation of Monte Carlo multi-group and continuous cross section. Ann. Nucl. Energy **127**, 433–436 (2019). https://doi.org/10.1016/j.anucene.2018.12.032
45. L. Deng, G. Li, B.Y. Zhang et al., A high fidelity general purpose 3-D Monte Carlo particle transport program JMCT3.0. Nucl. Sci. Tech. **33**, 108 (2022). https://doi.org/10.1007/s41365-022-01092-0
46. R. Macfarlane, D.W. Muir, R.M. Boicourt et al., The NJOY nuclear data processing system, Version 2016. (2017). https://doi.org/10.2172/1338791
47. R.D. Mosteller, F.B. Brown, B.C. Kiedrowski, An expanded criticality validation suite for MCNP. (2011). https://www.osti.gov/biblio/1083139
48. N.E. Agency, ICSBEP Handbook 2019. (2019). https://doi.org/10.1787/e2703cd5-en
49. K. Fan, Y.P. Yin, L.L. Song et al., Cross-Evaluation of the PU-MET-FAST criticality benchmark experiments in ICSBEP handbook (by the end of 2022). Nucl. Eng. Des. **415**, 112693 (2023). https://doi.org/10.1016/j.nucengdes.2023.112693
50. https://github.com/mit-crpg/benchmarks/tree/master/icsbep